VOL. 11, NO. 23, DECEMBER 2016 ISSN 1819-6608
ARPN Journal of Engineering and Applied Sciences
©2006-2016 Asian Research Publishing Network (ARPN). All rights reserved.
www.arpnjournals.com

# SIMULATIONS OF BREAST CANCER IMAGING USING 16-CHANNEL MAGNETIC INDUCTION TOMOGRAPHY

B. Gowry, Abu B. Shahriman and Z. Zulkarnay
Department of Biomedical Electronic Engineering, School of Mechatronic Engineering, Universiti Malaysia Perlis Campus Pauh Putra, Arau, Perlis, Malaysia
E-Mail: gowry@studentmail.unimap.edu.my

## ABSTRACT

In order to reduce the physical trauma caused by breast compressions, exposure to radiations and the high price of diagnostic tests, a new cost effective magnetic induction tomography (MIT) system is proposed to identify and locate tumors among the heterogeneous breast tissues. This technique operates in a non-invasive and contactless manner with the breasts. The numerical simulation imaging system consists of 16 sensor coils with 1 coil acting as the transmitter and the rest as receivers at a single time period, leading to a total of 240 receiver readings. The receiver readings and 240 generated sensitivity matrices were then used to reconstruct the images of the breast using linear back projection (LBP) algorithm after a careful comparison has been made on the algorithm with newton one-step error reconstruction (NOSER) and truncated singular value decomposition (TSVD) algorithms. The reconstructed images were assessed in terms of three essential error metrics which are the resolution (RES), magnification (MAG), and the position error (PE). The average errors are 0.004728, 13.7793, and 45.1929 for the RES, MAG and PE metrics respectively. Nonetheless, the average error metric values for the images of tumors located deepest, at the origin (0, 0), show better results in terms of PE that is -2.5356. A strong correlation between the MIT sensor readings and the size of simulated breast tumor was also observed from the adjusted R square value which is 0.998, indicating that the data fitted are very close to the regression line. The obtained results verify that the proposed MIT design and image reconstruction algorithm provide a promising alternative for breast cancer imaging although further studies are required to validate the simulation MIT data.

**Keywords:** magnetic induction tomography, breast cancer, numerical simulations, LBP, image error metrics, regression line.

## INTRODUCTION

Breast cancer is a throbbing sickness that no longer needs an introduction. This is especially true among ladies because of their unique breast structure that has more breast tissues when compared with that of man's. It is been anticipated that in 2016, at least 249260 new cases of breast cancer diagnosis and 40890 deaths will be accounted for [42]. In Malaysia, around 5000 ladies are determined to have the disease annually where almost 50% of them are under 50 years of age [43]. Aside from late diagnosis due to the lack of awareness of the disease, the reason adding to the huge figure could be because of current restrictions emerging from modalities like the magnetic resonance imaging (MRI), ultrasound and X-beam mammography [1]. New procedures which have the potential to defeat the constraints of the traditional gold standard breast tumor imaging methodology, depend upon the alterations in the electrical properties and subsequently, the electrical impedance of the breast tissues due to the vicinity of high vasculature in the presence of malignancies [2].

This has recommended the electrical impedance tomography (EIT) which infuses a significantly little amount of alternating current into the body through an array of electrodes [3]. On the other hand, the disadvantages of EIT are mistakes gotten by poor skin to electrode contact, the inability to know the accurate area of terminals because of human body surface variability, and, the certain very sensitive parts of the body [4]. In conjunction to that, a method proposed to overcome the electrode placement errors would be the non-tactile MIT [3]. The operation of MIT is initialized when a transmitter coil introduces a primary magnetic field into the breast tissue, thereby also inducing some electrical currents in the receiver coil as a function of magnetic induction. A perturbation of the primary magnetic field, the secondary field, will be generated upon transmission through the electrically conductive medium of the breast and tumor volumes. Therefore, a voltage difference that is derived from both the aforementioned magnetic signals collected from the receiver coil, estimates the inductive phase shift which denotes the malignancy status of the breast [4].

In recent years, MIT has been a success in imaging non-medical applications like the imaging of steel in reinforced concrete [5] , in the oil and gas industry [6], and, in the two phase flow imaging [7]-[8]. However, very few have been reported to date on its application in imaging biological tissues or in the medical field. Among them is in [9], where the authors came up with an improvised NOSER technique for the reconstruction of three-dimensional (3D) phantom images . The improvement was made on the Hessian matrix that is based on the Jacobian matrix (generally ill-conditioned for most MIT and EIT modalities). Singular value decomposition (svd) method was used to first determine the condition number, which denotes the extent to which the Jacobian matrix is ill conditioned. Then, the diagonal element of one of the three decomposed matrices is altered and the product of the new inverse matrices is obtained to get the improvised Hessian matrix. The proposed NOSER algorithm was found to have the best correlation coefficient of 98.22%, with the Tikhonov regularization 80.33%, and NOSER 85.68%. The algorithm proposed in the paper also showed better resolution and anti-noise

©2006-2016 Asian Research Publishing Network (ARPN). All rights reserved.


characteristics. Dekdouk, in his thesis, mentioned about MIT applications in lung ventilation and heart monitoring [6]. In his work, he applied TSVD and Tikhonov regularization methods.

MIT of a realistic 3D bio-impedance head model with a new linear image reconstruction algorithm was developed via an optimization process to obtain the best mapping between the training parameters set, and, their respective measurements from the forward solution of the finite element problem in [10]-[11]. The 3D model of the human head was derived from a set of magnetic resonance (MR) images. The proposed reconstruction method, when compared with the single-step regularized Gauss-Newton method [12], has reduced the reconstructed image error by 15%. A realistic peripheral cerebral haemorrhage with 12 tissue types was detected by a hemispherical MIT helmet 46-coil system in [13]-[14]. The simulation works were done using Comsol Multiphysics software at frequencies, 1 and 10 MHz. The resulting images were reconstructed using one-step Tikhonov regularized algorithm, with Gaussian phase noise added to the system. Zolgharni and team then extended the work by adding errors due to a displacement of the head and the size scaling. The results showed that a sufficiently good image could be obtained when the noise level, the displacement, and the scaling error are within 3 m degree, 3-4 mm and 3-4 %, respectively [12]-[13]. Wei and Wilkinson, in their paper developed the circuitry for a multichannel MIT data acquisition system. The novel design included a shielded coil structure with an integrated current measurement and a single-chip solution for the I/O demodulation. A maximum phase shift was observed to be around 2.5 at 10 MHz for the saline solutions with conductivity range akin to of biological tissues [15].

In 2004, MIT of low conducting materials were simulated and experimentally validated. The image reconstruction algorithm used was TSVD [16]. A regularized single step Gauss-Newton inverse solution was implemented for a MIT system with 16 excitation coils and 32 receiver coils. Four different regularization matrices were compared: identity matrix (IM), neighborhood matrix (NM), TSVD and variance uniformization (VU). The VU method outperformed all other methods with respect to the localization accuracy, the resolution and the edge sharpness, but, on the other hand, produced a larger variance in the images [17]. In [18], the inverse problem was solved using Tikhonov regularization technique for a 16- channel MIT system operating at 10 MHz. The MIT system was designed primarily for imaging biological tissues having conductivity values lesser than $10\,Sm^{-1}$. The average induced phase shift attained in this system is 17 m degrees [18]. Motivated by the previous works done on MIT for biological tissues, our team has proposed a 16-channel MIT system for imaging the breast tumor using LBP image reconstruction algorithm. This study is an extension of our work in [19], using the frequency with the best results in [19], and a higher number of transceivers for tissue imaging purposes. In [19], our team has made a comparative study with [2], to detect breast cancer using magnetic induction spectroscopy (MIS) technique. In this study, we have concluded that our proposed coil configuration has a higher inductive phase shift intensity, which denotes the presence and absence of a breast tumor.

## METHODS: FINITE ELEMENT SIMULATION

This section describes the developed two dimensional (2D) MIT setup model with the finite element method and simulation criteria involved. The feasibility of the magnetic induction concept in detecting breast tumors in a non-invasively and non-tactile manner is also explained. Figure-1 shows the flow chart of the overall work done in this paper.

### Numerical simulation model

The simulation model consists of 16 transceiver sensor coils (circles) with 1 coil acting as the transmitter (excited by 1 A) and the rest acting as receivers at a single time period. The rectangle speaks to the insulator (i.e., air), while the ellipses, two greater and one smaller circles represent the breast fibro-glandular ,fat , skin and tumor tissues individually (refer to Figure-1). The improvement made in this study in terms of the numerical breast model, is the realistic non-uniform heterogeneous breast tissue model (scattered fibro-glandular tissues within the fat layer) [34]. Although most previously developed breast models for other breast cancer diagnosing techniques are in 3D [35]-[38], the multilayer tissues are uniformly arranged which can lead to certain deviations in the actual scenario involving patients. This is especially true when the tumor overlaps with normal breast tissues.

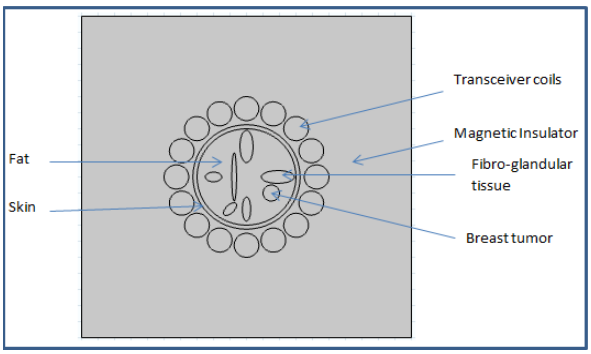


**Figure-1.** 2D MIT system and a multilayer breast tissue model.

ARPN Journal of Engineering and Applied Sciences
©2006-2016 Asian Research Publishing Network (ARPN). All rights reserved.


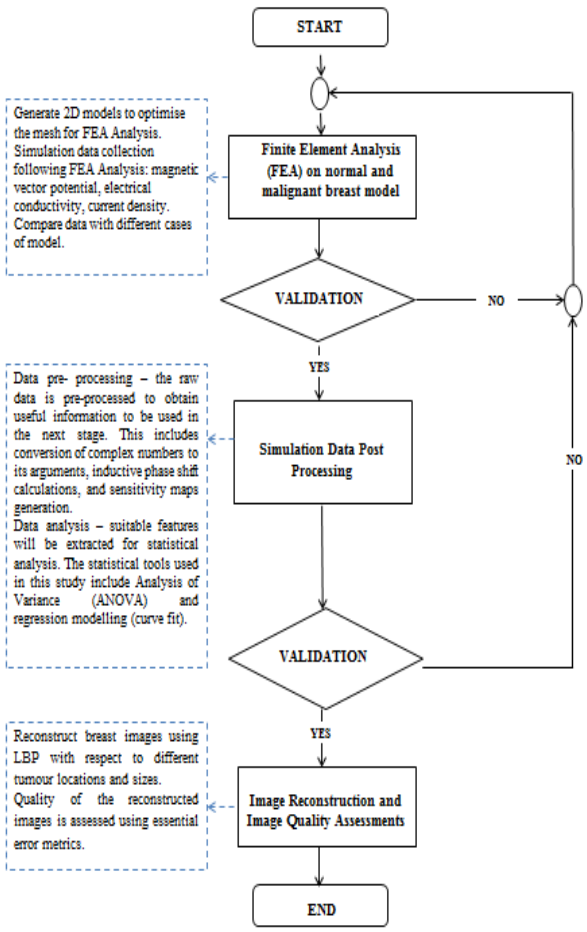


**Figure-2.** Flow chart of the methodology.

**Finite element method and simulation criteria**

The workstation used for the simulation works comprises of a Dell Inspiron PC with an i5 processor and 8GB RAM. In Comsol, a triangular cross section with a linear and iterative solver was utilized. The default solver relative resilience is 0.001. Table-1 presents the parameters included in the study. The estimations of the conductivity and permittivity of the typical human breast tissues and tumor tissue are taken from [2] [31]. The 10 MHz frequency, with which the simulations are led, is purposely chosen to be in the β scattering locale where most pathological changes occur [19]-[20], [13]-[15], [18]. In the meantime, a time harmonic and quasi-static assumption, Equation (1), was additionally made in the Ampere's equation utilized in Comsol to produce the magnetic vector potential distribution in the model. As such, the displacement current streams in the Ampere's mathematical statement were disregarded, and a non-moving geometry was considered with no external electric potential gradient.

$$(\sigma j\omega - \omega^2\varepsilon)A + \nabla \times (\mu^{-1}(\nabla \times A)) = J_e \qquad (1)$$

where $\mu$ is the medium permeability (henry/meter) and $\varepsilon$ is the medium permittivity (farad/meter), $\sigma$ is the medium conductivity (siemens/meter), $\omega$ is the angular frequency, $J_e$ is the external electric current density (ampere/ meter$^2$), and $A$ is the magnetic vector potential( $\vec{A}$ ).

**Table-1.** List of parameters of the simulation model.

| Parameters | Values |
|---|---|
| Number of turns of coils | 5 |
| Current applied at coils | Excitation coil: 1 A<br>Detecting coils: 0 A |
| Coil type | Linear |
| Coil material | Copper |
| Diameter of coils | 0.015 m |
| Diameter of breast fat | 0.06 m |
| Thickness of skin tissue | 0.005 m |
| Size of insulator | 0.4 m * 0.4 m |
| Frequency used | 10 MHz |
| Di-electrical properties of the breast fat tissue | Conductivity: 0.02806 S/m<br>Permittivity: 7.8933 |
| Di-electrical properties of fibro-glandular tissue | Conductivity: 0.71954 S/m<br>Permittivity: 162.73 |
| Di-electrical properties of skin (dry) | Conductivity: 0.197323 S/m<br>Permittivity: 361.670349 |
| Di-electrical properties of the breast tumor tissue | Conductivity: 8.2 mS/m<br>Permittivity: 300 |

©2006-2016 Asian Research Publishing Network (ARPN). All rights reserved.


**Magnetic induction concept**

The tumor of the breast tissue could be distinguished using magnetic induction when electrical waves are transmitted to one of the sensor coils (transmitter) of the tomography framework, producing an attractive field around the coil as per the Ampere's law (refer to Figure-3). This attractive magnetic field when going through the heterogeneous breast tissues and tumor thus impels the perturbed eddy current present as an element of di-electrical properties that exist in the tissues and also in the rest of the sensor coils (receivers), restricting the change that is brought on it. This also complies with Lenz's and Faraday's law of induction, Eq. (2):

$$\varepsilon = -\frac{\partial \phi}{\partial t} \tag{2}$$

where $\varepsilon$ is the induced voltage, the negative sign signifies the direction, and $\partial \phi$ is the adjustment in the magnetic flux created.

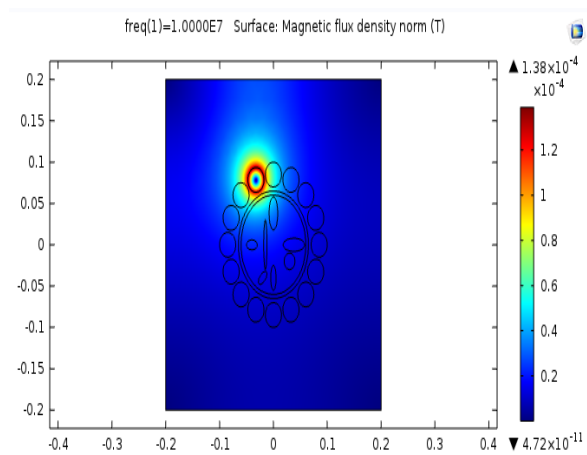


**Figure-3.** Simulation output resulting from excitation of the 16th sensor.

The subsequent inductive phase shift, which indicates the presence and absence of a tumor, depends on the distinction in the power of the induced voltage identified at the receiving coils. In Comsol, the induced voltage, $V_{mn}$ observed when transceiver m is activated and transceiver n acts as a receiver, is evaluated by performing a surface integration of the product of the current density and magnetic vector potential at the receiver coils utilizing the mathematical statement given as part of [8], Eq. (3):

$$V_{mn} = -j\omega \int_{\Omega_c} A_{\bullet} J_0 dS \tag{3}$$

where $A$ and $J_0$ are the magnetic vector potential and current density passing through the coil respectively. While the normalized induced voltage phase shift is calculated using Eq. (4):

$$\Delta V = \frac{V_{mn} - V_{ref}}{V_{ref}} \tag{4}$$

where $V_{ref}$ is the $V_{mn}$ when the simulation is done on only coils, without the breast tissues for normal breast tissues phase shift readings, and, it is the $V_{mn}$ when the simulation is done on the breast tissues without the presence of tumor tissue (normal) for breast tissue with the presence of tumor phase shift reading calculations.

## METHODS: IMAGE RECONSTRUCTION

**Sensitivity matrix calculation**

The sensitivity grid map for a given sensor setup is an essential step in the inverse part of every forward simulation problem. The sensitivity matrix, *S*, shapes a premise set from which image vectors can be acquired [21]-[22]. Fundamentally, every pixel of S speaks to the effect of the sensor framework to every conductivity pixel in a uniform distribution of sample [23]:

$$S = \frac{\partial V_{mn}}{\partial \sigma_k} = -\omega^2 \frac{\int_{\Omega_k} A_m \cdot A_n \partial v}{I_0} \tag{5}$$

where $V_{mn}$ is the voltage reading, $\sigma_k$ is the conductivity of pixel *k*, $\Omega_k$ is the area of the perturbation *k*, $A_m$ and $A_n$ are magnetic vector potential solutions when the excitation coil $m$ is excited by $I_0$ and when the sensing coil $n$ is excited with unit current, respectively.

The sensitivity matrix is carefully construed in accordance to Eq. (5) and is then generated in MATLAB; refer to Figure-4. The following are the procedures to construct a single sensitivity map:

**Step 1:** Excite every sensor one at a time, and store the resulting Comsol simulation data of magnetic vector potential in the form of a 128*128 pixels grid. The arguments of the complex magnetic vector potential are obtained using the equation provided in [3].

**Step 2:** Compute the dot product of the magnetic vector potential maps for each and every transceiver pair (Total number of pairs: 16 transmitters * 15 receivers = 240 matrix).

**Step 3:** Sum all the matrix generated in Step 2. The final matrix is called the weight balance map (WBM).

©2006-2016 Asian Research Publishing Network (ARPN). All rights reserved.


**Step 4:** Normalize each sensitivity matrix (matrices generated in Step 2) by dividing it by the maximum pixel intensity, *Pm* of WBM.

**Image reconstruction algorithms**

There are numerous image reconstruction algorithms, for example, linear back-projection, nonlinear algorithms, and filtered back projection; however, in this article, only the LBP, NOSER and TSVD algorithms are utilized as they have become well-known techniques among analysts due to their low computation requirements and their basic and quick response as an algorithm.

**LBP**

The LBP calculation is based on the product of multiple matrices. Keeping in mind that the end goal is to reproduce the forward solution, each sensitivity map is multiplied by its relating sensor reading and summed. Although LBP produces blurred images with artifacts and 1/r image roll offs, it is still the fastest compared to other more accurate techniques [24]. The mathematical equation of LBP is stated in Equation (6).

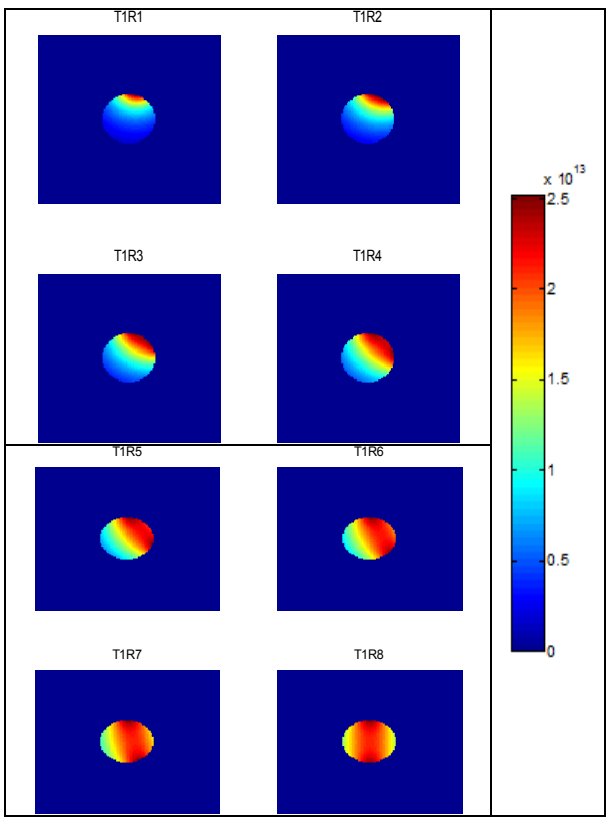


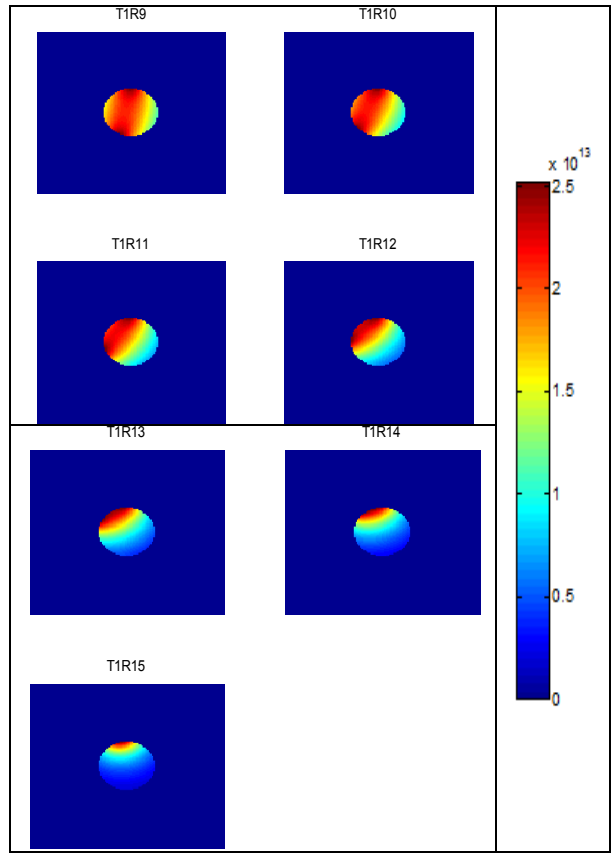


**Figure-4.** Sensitivity maps of transmitter 1 with corresponding receivers (T1R1-T1R15).

$$V_{LBP}(x,y) = \sum_{Tx=0}^{8}\sum_{Rx=0}^{7} S_{Tx,Rx} X\overline{M}_{Tx,Rx}(x,y) \tag{6}$$

where, $V_{LBP}(x,y)$ is the voltage distribution obtained using LBP algorithm in n x n matrix where n is equals to dimension of sensitivity maps, $\overline{M}_{Tx,Rx}(x,y)$ is the induced voltage phase shift in $Rx^{th}$ sensor coil for $Tx^{th}$ projection, $S_{Tx,Rx}$ is the normalized sensitivity matrices for the view of *Tx-Rx*.

**NOSER**

NOSER algorithm which is a derivative of the common iterative Newton-Raphson calculation is based on the least squares theory. NOSER algorithm estimates the conductivity distribution of the resulting images by utilizing only one step of the Newton's method thereby reducing the computational time. The single step is done by calculating the sensitivity matrix (also known as Jacobian matrix) just once and then modifying it by means of parameter λ and matrix R [9]. The NOSER formula [9] is

©2006-2016 Asian Research Publishing Network (ARPN). All rights reserved.


$$\Delta\sigma = [Hessian]^{-1} * \sum_{Tx=0}^{8}\sum_{Rx=0}^{7} S_{Tx,Rx} X\overline{M}_{Tx,Rx}(x,y) \quad (7)$$

where $Hessian = S_{Tx,Rx} * S_{Tx,Rx}{}^{T}$, $S_{Tx,Rx}$ is the normalized sensitivity matrices for the view of *Tx-Rx*, $\overline{M}_{Tx,Rx}(x,y)$ is the corresponding induced voltage phase shifts in the receiver coils.

**TSVD**

Truncated singular value decomposition is a famous regularization technique used to alter certain ill-conditioned sensitivity matrices that are singular or have very small values. The sensitivity matrix generated in section 3.1 is first decomposed into three constituent matrices which are U, W and Y'. The diagonal elements of W ($w_i$) are the singular values which are set to zero when they have very small values, depending on the condition number of the ill-conditioned sensitivity matrix [16]. The conductivity distribution is estimated by taking the inverse of the altered decomposed elements using

$$\Delta\sigma = \overline{Y}[diag(1/w_i)]\overline{U}^T\overline{M} \quad (8)$$

where $\overline{Y}$ is a *n x n* unitary matrix, $\overline{U}$ is a *m x n* unitary matrix, $\overline{M}$ is the corresponding induced voltage phase shifts in the receiver coils.

**METHODS: QUALITY ANALYSIS OF THE RECONSTRUCTED IMAGES**

In order to measure the quality of the reconstructed images, several analyses have been performed. The images were assessed in terms of resolution, magnification, position error, shape deformation, peak signal to noise ratio as well as mean structural similarity index. The first four assessments were originally proposed for EIT modality which are based on GREIT standard [23]; however, they have also been applied in MIT applications [24]-[26].

**Resolution (RES)**

RES measures the proportion of reconstructed tumors with respect to the entire medium and is expressed as

$$RES = \sqrt{\frac{A_q}{A_0}} \quad (9)$$

where $A_q$ is the number of pixels covered by the reconstructed tumor and $A_o$ is the number of pixels covering the entire medium of reconstruction. The RES should be uniform and small to represent a target more accurately in the conductivity distribution

**Magnification (MAG)**

MAG is used to compare the size of the reconstructed tumor, RES (*q*) with the actual size of tumor/target, RES (*t*). If MAG is equals to 1, then the size of the reconstructed image is identical to the original image. Refer Equation (10).

$$MAG = \frac{RES(q)}{RES(t)} \quad (10)$$

**Position Error (PE)**

PE determines the extent to which the reconstructed tumor represents the actual tumor or target location. An acceptable PE should be small and vary less for every tumor positions. Depending on the target, $r_t$ and reconstructed tumor, $r_q$ position from the centroid of the whole image, region of interest (ROI), PE is expressed as in Equation (11)

$$PE = r_t - r_q \quad (11)$$

where $r_t$= distance of target from center of ROI/radius of ROI.

**Shape deformation (SD)**

SD measures the extent to which a reconstructed tumor follows the shape of the circular target. This is done by dividing the number of reconstructed tumor pixels, $A_o$ outside a circle, which is of equivalent area, with the number of pixels covering the entire reconstructed tumor region, $A_q$. A good quality set of images has low and uniform SD, refer Equation (12).

$$SD = \frac{Ao}{Aq} \quad (12)$$

**Peak Signal to Noise Ratio (PSNR)**

The PSNR calculates in decibels, the peak of signal-to-noise ratio between the reference image and reconstructed image. The good quality of the reconstructed image is determined by the higher value of PSNR. In order to measure PSNR (peak error), MSE that is the measure of cumulative squared error between two images is computed first. The error is said to be less when MSE is low. Refer Equation (13) and Equation (14).

$$MSE = \frac{\sum_{M,N}[I_1(m,n) - I_2(m,n)]^2}{M * N} \quad (13)$$

where, *M* and *N* are the number of rows and columns in the input images, respectively.

©2006-2016 Asian Research Publishing Network (ARPN). All rights reserved.


$$PSNR = 10\log_{10}(\frac{R^2}{MSE}) \tag{14}$$

where, $R$ is the maximum fluctuation in the input image data type.

**Mean Structural Similarity Index (MSSIM)**

MSSIM is used to compare the similarity between reference image and the reconstructed image in terms of its structure, luminance as well as contrast. MSSIM is equals to one when the reconstructed image exactly replicates the true image. Eq. (15) and Eq. (16) represent the mathematical definition of MSSIM

$$MSSIM(X,Y) = \frac{1}{M}\sum_{j=1}^{M} SSIM(x_j, y_j) \tag{15}$$

$$SSIM(x,y) = [l(x,y)]^{\alpha}[c(x,y)]^{\beta}[s(x,y)]^{\gamma} \tag{16}$$

where $X$ is the reference image, $Y$ is the reconstructed image, $x$ and $y$ are the image contents at the $j^{th}$ local window, $M$ is the total number of local windows, $l$, $c$, and $y$ are the luminance, contrast and structural comparison function with $\alpha$, $\beta$ and $\gamma$ being the parameters to adjust their relative importance respectively.

## METHODS: PARAMETRIC STATISTICAL ANALYSIS

Curve fit regression modeling is a tool used to fit the data of interest to a model. The accuracy of the fit is then analyzed in terms of R-squared value and coefficients. The independent variables or parameters, of the data, are known as the predictors while the dependent variables as the responses [32]. In this study, the predictors are the size of tumor and the responses are the corresponding sensor readings. The descriptive analysis tool that is also used in this study is ANOVA, an extension of the *t* and *z*-test, which is a statistical method for analysis of variance. The *t*-test, however, cannot be used in this study as it is not applicable for more than two groups. In this work, this analysis is done to obtain the statistical significance of the MIT sensor coil readings in differentiating the size of the breast cancer. The features or readings that are truly significant will have F and p-value that reject the null hypothesis. The null hypothesis simply assumes that if the probability (p-value) is greater than 0.05 and the F value is less than or equals to 1, then the features are not significant. The significance in here means that the features are not similar and are able to be utilised to differentiate between classes. The results of the aforementioned analysis are shown in the section 7.

## RESULTS AND DISCUSSIONS

The results in this study are presented in two parts. The first part discusses the results of the analysis works done using 8-channel, MIT (half the number of sensors used in the proposed system) while the second part is on the analyses done using the proposed system that is the 16-channel MIT. The comparative system analysis is done on the 8-channel MIT system prior to the proposed system. This is to determine the reliability of the proposed concept and the best reconstruction algorithm to be used for the 16-channel MIT, as it reduces the computational time and system complexity significantly, without having to be analyzed on the proposed system directly.

### Eight-channel MIT

**MIT sensor array activation profile**

Table-2 shows the readings of the transceiver sensor coils derived from the Comsol simulations for different cases in terms of induced voltage (IV), as well as the inductive phase shift (IPS) calculations. Since the IV profiles are the same for every case, only the normal case IV profile is shown. The receiver readings for each case are tabulated in such a way that the first receiver reading for every excitation (transmitter 1-8), is calculated from the sensor adjacent to the sensor being excited by 1A [2]-[3]. This is followed by the remaining sensors according to the sequence shown in Figure-3. The top most profile presented is the IV readings in terms of voltage, V, for the normal breast tissue case model (without tumor tissue presence). The readings are the lowest for the neighboring sensors and the highest for the sensors located furthest from the transmitting sensor. This is due to the very low magnetic vector potential and current density distribution which are detected at the receiving sensor coils that it falls in the negative range of values, since the tissues being imaged are also of very low conductivity values. Thus, although the initially detected individual aforementioned parameters are significantly highest for the adjacent sensors as they are the closest to the transmitting coil, they become the lowest once the readings are computed in terms of IV.

On the other hand, the IPS measurement profiles for the normal breast tissue with and without the center positioned tumor are almost similar to one another as the imaging object are both placed at the center of the MIT system. Therefore, only receiver readings number 3, 4 and 5 of the system which are at the opposite side of the transmitting sensors consistently show higher readings than the rest of the sensors. This suggests that the imaging objects are almost exactly or exactly overlapping on the pathway of the signal transmitted to the receiver coils, thereby inducing a delay in the received signals that is interpreted as IPS in this study. A similar pattern is observed for the remaining case profiles, where a higher IPS is reflected at the receiving ends which the pathway of transmission is obstructed or perturbed by the presence of tumor(s).

ARPN Journal of Engineering and Applied Sciences
©2006-2016 Asian Research Publishing Network (ARPN). All rights reserved.


**Table-2.** MIT sensor array activation profiles.

| | | | | Receiver | | | |
|---|---|---|---|---|---|---|---|
| **Transmitter** | **1** | **2** | **3** | **4** | **5** | **6** | **7** |
| 1 | 1.6746 | 4.6856 | 7.5192 | 8.9541 | 7.5405 | 4.3994 | 1.6368 |
| 2 | 1.6431 | 4.3022 | 7.3712 | 8.6981 | 7.3317 | 4.4180 | 1.6746 |
| 3 | 1.5664 | 4.3636 | 7.4460 | 8.7385 | 7.5623 | 4.6856 | 1.6431 |
| 4 | 1.4717 | 4.1691 | 7.0301 | 8.4431 | 7.5192 | 4.3022 | 1.5664 |
| 5 | 1.5608 | 4.2193 | 7.2325 | 8.9541 | 7.3712 | 4.3636 | 1.4717 |
| 6 | 1.4801 | 4.1720 | 7.5405 | 8.6981 | 7.4460 | 4.1691 | 1.5608 |
| 7 | 1.4586 | 4.3994 | 7.3317 | 8.7385 | 7.0301 | 4.2193 | 1.4801 |
| 8 | 1.6368 | 4.4180 | 7.5623 | 8.4431 | 7.2325 | 4.1720 | 1.4586 |
| **Description** | **Normal breast tissue (IV)** | | | | | | |
| 1 | 2.02E+13 | 1.90E+14 | 5.91E+14 | 8.83E+14 | 5.93E+14 | 1.78E+14 | 1.97E+13 |
| 2 | 1.98E+13 | 1.71E+14 | 5.80E+14 | 8.42E+14 | 5.76E+14 | 1.76E+14 | 2.02E+13 |
| 3 | 1.89E+13 | 1.77E+14 | 5.85E+14 | 8.62E+14 | 5.95E+14 | 1.90E+14 | 1.98E+13 |
| 4 | 1.77E+13 | 1.66E+14 | 5.53E+14 | 8.17E+14 | 5.91E+14 | 1.71E+14 | 1.89E+13 |
| 5 | 1.88E+13 | 1.71E+14 | 5.69E+14 | 8.83E+14 | 5.80E+14 | 1.77E+14 | 1.77E+13 |
| 6 | 1.78E+13 | 1.66E+14 | 5.93E+14 | 8.42E+14 | 5.85E+14 | 1.66E+14 | 1.88E+13 |
| 7 | 1.76E+13 | 1.78E+14 | 5.76E+14 | 8.62E+14 | 5.53E+14 | 1.71E+14 | 1.78E+13 |
| 8 | 1.97E+13 | 1.76E+14 | 5.95E+14 | 8.17E+14 | 5.69E+14 | 1.66E+14 | 1.76E+13 |
| **Description** | **Normal breast tissue (IPS )** | | | | | | |
| 1 | 0.0027 | 0.0036 | 0.0046 | 0.0049 | 0.0046 | 0.0037 | 0.0027 |
| 2 | 0.0027 | 0.0038 | 0.0047 | 0.0050 | 0.0047 | 0.0038 | 0.0027 |
| 3 | 0.0028 | 0.0038 | 0.0046 | 0.0050 | 0.0046 | 0.0036 | 0.0027 |
| 4 | 0.0029 | 0.0039 | 0.0048 | 0.0051 | 0.0046 | 0.0038 | 0.0028 |
| 5 | 0.0028 | 0.0039 | 0.0047 | 0.0049 | 0.0047 | 0.0038 | 0.0029 |
| 6 | 0.0029 | 0.0039 | 0.0046 | 0.0050 | 0.0046 | 0.0039 | 0.0028 |
| 7 | 0.0029 | 0.0037 | 0.0047 | 0.0050 | 0.0048 | 0.0039 | 0.0029 |
| 8 | 0.0027 | 0.0038 | 0.0046 | 0.0051 | 0.0047 | 0.0039 | 0.0029 |
| **Description** | **Breast tissue with tumor at (0,0) coordinate (IPS)** | | | | | | |
| 1 | 0.0020 | 0.0041 | 0.0059 | 0.0045 | 0.0028 | 0.0018 | 0.0011 |
| 2 | 0.0044 | 0.0069 | 0.0059 | 0.0043 | 0.0032 | 0.0024 | 0.0020 |
| 3 | 0.0081 | 0.0073 | 0.0060 | 0.0051 | 0.0044 | 0.0041 | 0.0044 |
| 4 | 0.0068 | 0.0059 | 0.0056 | 0.0056 | 0.0059 | 0.0069 | 0.0081 |
| 5 | 0.0031 | 0.0032 | 0.0037 | 0.0045 | 0.0059 | 0.0073 | 0.0068 |
| 6 | 0.0015 | 0.0020 | 0.0028 | 0.0043 | 0.0060 | 0.0059 | 0.0031 |
| 7 | 0.0011 | 0.0018 | 0.0032 | 0.0051 | 0.0056 | 0.0032 | 0.0015 |
| 8 | 0.0011 | 0.0024 | 0.0044 | 0.0056 | 0.0037 | 0.0020 | 0.0011 |
| **Description** | **Breast tissue with tumor at (0.03,-0.02) coordinate (IPS)** | | | | | | |
| 1 | 0.0046 | 0.0077 | 0.0106 | 0.0094 | 0.0074 | 0.0055 | 0.0038 |
| 2 | 0.0072 | 0.0108 | 0.0106 | 0.0093 | 0.0078 | 0.0062 | 0.0046 |
| 3 | 0.0109 | 0.0111 | 0.0106 | 0.0100 | 0.0091 | 0.0077 | 0.0072 |
| 4 | 0.0098 | 0.0098 | 0.0104 | 0.0107 | 0.0106 | 0.0108 | 0.0109 |
| 5 | 0.0060 | 0.0071 | 0.0084 | 0.0094 | 0.0106 | 0.0111 | 0.0098 |
| 6 | 0.0044 | 0.0059 | 0.0074 | 0.0093 | 0.0106 | 0.0098 | 0.0060 |
| 7 | 0.0040 | 0.0055 | 0.0078 | 0.0100 | 0.0104 | 0.0071 | 0.0044 |
| 8 | 0.0038 | 0.0062 | 0.0091 | 0.0107 | 0.0084 | 0.0059 | 0.0040 |
| **Description** | **Breast tissue with tumors at (0.03,-0.02) and at (0,0) coordinates (IPS)** | | | | | | |

Moreover, the maximum IPS is 8.05 m degrees for single breast tumor detection. This value is lesser than those reported in [15] and [18] as the tissues being imaged in their studies are of higher conductivity values. Hence, the magnetic induction phenomenon occurs at a higher rate and subsequently yields a higher maximum IPS reading.

**Reconstructed images using LBP, NOSER and TSVD algorithms**

Figure-5 represents five different conductivity profiles of the true imaging model described in section 2. Figure 5 (a) illustrates the tumor at center position (0, 0) while (b), (c), (d) and (e), at coordinates (0.04, 0), (-0.03, 0.04), (-0.04,-0.01) and (-0.03,-0.04), respectively.

ARPN Journal of Engineering and Applied Sciences
©2006-2016 Asian Research Publishing Network (ARPN). All rights reserved.


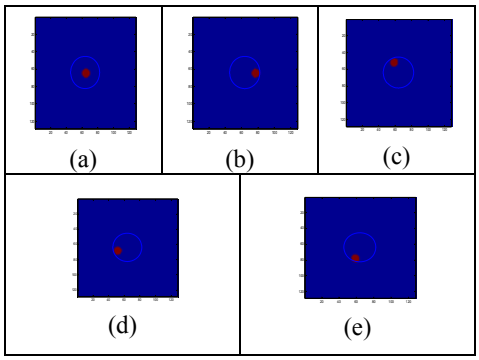


**Figure-5.** True breast model images.

Meanwhile, the reconstructed images are shown in Figure 6. The images are arranged in a 5 x 3 matrix manner whereby the rows determine the tumor positions as per described and arranged in Figure-5, while the columns denote the methods of image reconstruction used. The first column of images is generated using LBP algorithm, followed by NOSER and TSVD. Upon reconstruction using the aforementioned methods, the images of tumors at distinct positions were normalized and subtracted from the normal breast tissue image. The resulting images were then subjected to a threshold value in order to obtain binary final images as shown in Figure-6. The threshold value for the binary normalized images was set to 0.01 for LBP reconstructed images and 0.001 for the other two reconstruction algorithms based on empirical observations. However, only for Figure-6 (a), (f), and (k), the normalization is done after subtraction as the usual way gives a diverged image (outside of ROI).

Based on Figure-6, it shows evidently that the best technique in producing images that resemble the original images from Figure-5 is LBP, followed by NOSER and TSVD. As for NOSER and TSVD techniques, the only images that resemble the target image almost perfectly are (h) and (m). NOSER (f) and TSVD (k) reconstructed images show the largest deviation from the original image for the tumor placed at the center, where (f) shows false positive indication of tumor presence (ones or red area) at two places in the ROI (breast tissue represented as a circle) while (k) shows no tumor presence. Figure-6 (n) and (o) also reflect some unreliability when using TSVD for our application. To further strengthen the findings and to assess the quality of the images, quality check results of the images have been discussed in the following section.

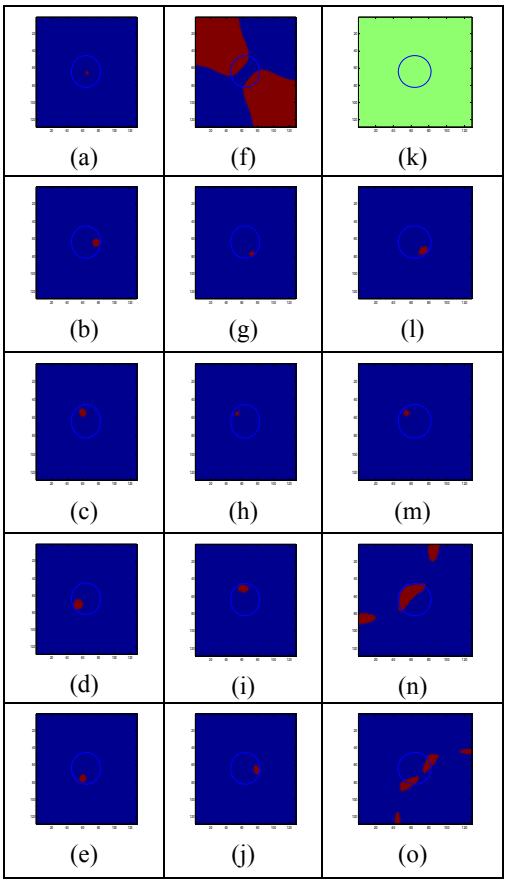


**Figure-6.** Reconstructed images. (a), (b), (c), (d), (e) reconstructed images when using LBP; (f), (g), (h), (i), (j) reconstructed images when using NOSER; (k), (l), (m), (n), (o) reconstructed images when using TSVD regularization method.

**Comparison of error metrics between image reconstruction algorithms**

Table-3 shows the results of error metrics based on six important qualitative parameters that are RES, PE, MAG, SD, PSNR and MSSIM. Figure-6 (a), (b), (c), (d) and (e) denote images reconstructed from LBP technique while (f), (g), (h), (i), (j) and (k), (l), (m), (n), (o) denote images reconstructed when using NOSER and TSVD techniques respectively. In accordance to the GREIT standard of image performance merits, the most important error metric among four GREIT parameters used in Table-3 is PE, followed by MAG, RES and SD. Not forgetting PSNR and MSSIM parameters which are equally important and widely used in [27]-[30].

ARPN Journal of Engineering and Applied Sciences
©2006-2016 Asian Research Publishing Network (ARPN). All rights reserved.


**Table-3.** Image error metrics results.

| Figure 6 | RES | PE | MAG | SD | PSNR | MSSIM |
|---|---|---|---|---|---|---|
| (a) | 0.0053 | 0 | 0.2105 | 0.25 | 24.3627 | 0.9834 |
| (b) | 0.0197 | -5.3726 | 0.8333 | 0.2 | 27.6726 | 0.9877 |
| (c) | 0.0204 | -11.1054 | 0.8493 | 0.127 | 20.8409 | 0.9683 |
| (d) | 0.0348 | -15.2875 | 1.4521 | 0.1509 | 19.8653 | 0.9704 |
| (e) | 0.0204 | 6.5728 | 0.8493 | 0.0967 | 25.6121 | 0.9844 |
| (f) | n/a | n/a | n/a | n/a | n/a | n/a |
| (g) | 0.0102 | -22.4189 | 0.4306 | 0.3226 | 22.0158 | 0.974 |
| (h) | 0.0069 | 6.3824 | 0.2877 | 0.1905 | 22.4129 | 0.9741 |
| (i) | 0.0299 | 30.1804 | 1.2466 | 0.3077 | 19.9958 | 0.9673 |
| (j) | 0.0174 | -24.1447 | 0.726 | 0.2264 | 21.1405 | 0.9692 |
| (k) | n/a | n/a | n/a | n/a | n/a | n/a |
| (l) | 0.0227 | -12.4268 | 0.9583 | 0.1594 | 20.8409 | 0.9733 |
| (m) | 0.0112 | 3.5662 | 0.4658 | 0.0588 | 21.8504 | 0.972 |
| (n) | n/a | n/a | n/a | n/a | n/a | n/a |
| (o) | n/a | n/a | n/a | n/a | n/a | n/a |

From Table-3, it can be proven that the images produced by LBP algorithm fulfill all of the criteria of a good quality image described in the previous sections as their RES,PE, and SD are small and uniform when compared to of NOSER's and TSVD's. Also, their PSNR is high with MAG and MSSIM approaching 1 for almost all of the images. The positive values of PE indicate that the reconstructed image is pushed to the centroid of ROI and vice versa [22]. On the other hand, NOSER images have double the PE value of LBP's when compared in terms of the images with highest PE values, -15.2875 (LBP) and 30.1804 (NOSER) respectively. The not applicable (n/a) signs are given to those images that give obvious false prediction of tumor locations as in Figure-6 (f), (k), (n), (o). In addition to that, NOSER images, although with consistently good RES, PSNR and MSSIM values, are not as good in representing the true images as its MAG and SD values are considerably inconsistent and higher when compared to of LBP images. MAG values that are smaller than one indicate that the reconstructed object is smaller than its actual size and vice versa for the values that are bigger than one.

As for the images reproduced by TSVD calculation, only two of the tumor positions are reconstructed with averagely good values of the aforementioned metrics. Therefore, it is very unlikely to be considered as a suitable image reconstruction technique for the detection and localization of breast tumor in this study.

**Sixteen- channel MIT**

The performance of the image reconstruction algorithms when compared, proved that the algorithm that has the best merits in all of the error metrics is the LBP, with an average of 5% (PE), 0.02 (RES), 0.84 (MAG), 0.16 (SD), 23.67 (PSNR) and 0.98 (MSSIM) respectively. Therefore, here we describe the results of six images that are reconstructed using LBP with the proposed 16 channeled MIT when the tumor numbers and locations are varied as shown in Figure-7.

**LBP based reconstructed breast MIT images**

Figure-7(a) shows the reconstructed image for tumor at (0,0) coordinate; (b), at (0.03,-0.02); (c), at (0,0) and (0.03,-0.02); (d), at (0.015,-0.02) and (0.015,0.02); (e), at (0.03,0.02) and (0.02,-0.03); (f), at (-0.03,0.02), (0.02,-0.03), and (0.03,0.027). Whereas, the true images are the adjacent images, from Figure-7 (g) to (l). The figure proves that the proposed MIT system can successfully locate and identify the position of tumors among the healthy breast tissues although not so accurately, as there are considerably large variances in terms of area difference, RES, PE and other error metrics when comparing the reconstructed images with the true images. This is mainly due to the lower number of sensors used to reduce the overall cost of production and maintenance in comparison with the ultrasound machines and high end conventional MRI that usually have hundreds of sensors.

By reducing the overall cost, this technology could be used as an adjunct along with the conventional imaging modalities or as a screening kit atleast in the rural areas where unavailabilty of essential expensive medical equipments could be a highly crucial problem. Other than that, the average computational scan time of the numerical system is approximately 5 minutes which is much lesser than of a typical MRI's which is about 45-60 minutes [41]. In the next section, the qualities of the reconstructed images are assessed in terms of the error metrics mentioned in Section 4.

ARPN Journal of Engineering and Applied Sciences
©2006-2016 Asian Research Publishing Network (ARPN). All rights reserved.


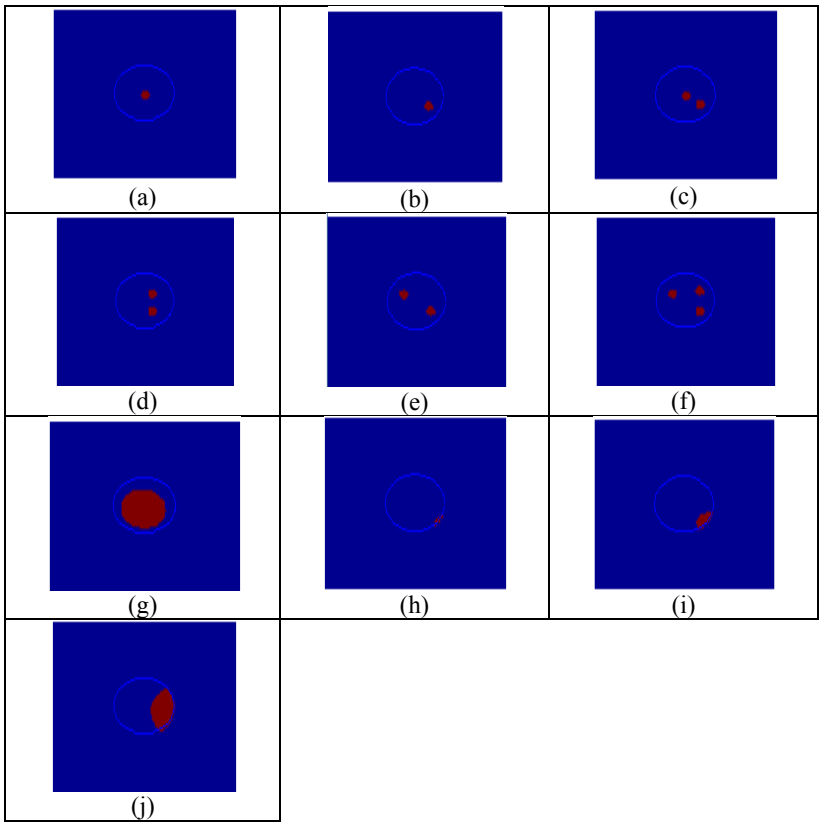


**Figure-7.** Breast images reconstructed using LBP algorithm.

**Image quality assessment**

In Figure-8, the results of 104 reconstructed images evaluated in terms of the three main error metrics which are the RES, MAG and PE, are shown. The 104 images are obtained with respect to 13 different sizes of tumor, each at 8 different locations in the region of interest. The size of tumors were incremented starting from 0.003 m to 0.015 m radius at a step size of 0.001 m, whereas, the locations of tumor of each size are varied between (0,0), (0.02,0), (0.04,0), (0,0.02), (0.02, 0.02), (0.04, 0.02), (0, 0.04), and (0.02, 0.04) coordinates. The smallest size of breast tumor chosen in this study is extremely small as the actual stage 1 breast tumor sizes are of 0.01 m radius or lesser [44]. The RES and MAG error metrics show almost consistent results with respect to different tumor sizes. However, it can be noticed that whenever the tumor is shifted to the central line (x=0 m), the values are significantly higher (more than 1), which is followed by tumors located away from the central line towards the sensor coils. This is proven in the previous Figure-7 (a), where the area of the reconstructed center tumor is the largest and highly enlarged when compared to the actual simulated tumor size.

As the sizes of tumors are increased, the values of the MAG metric decreases and the RES metric become smaller and more uniform. On the contrary, PE values are the least for tumor at (0, 0), although pushed away from the centroid of ROI (negative value). PE values at midline(x=0 m and different y values) is smaller than of tumor images located towards the far ends of the breast. The average errors for all of the images are 0.004728±0.007312, 13.7793±32.7322, and 45.1929±42.1299 for the RES, MAG and PE error metrics, respectively. Meanwhile, the average error metric values for images of tumor located at the origin (0, 0) show better results in terms of PE, that is -2.5356±4.5750. The trend of all of the error metrics discussed is similar to the ones reported in [23].

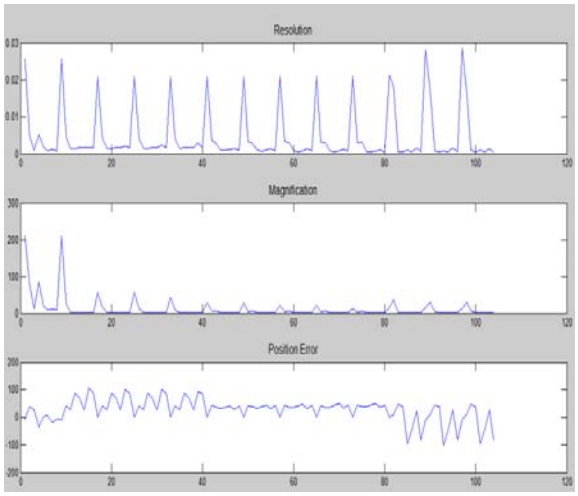


**Figure-8.** Error metrics plot for 16 channeled MIT.

ARPN Journal of Engineering and Applied Sciences
©2006-2016 Asian Research Publishing Network (ARPN). All rights reserved.


**Preliminary analysis: relationship between breast tumor size and MIT sensor IV readings**

This part of the paper discusses the results obtained from the analysis conducted to statistically correlate the relationship between the different breast tumor sizes and the corresponding IV readings. By doing so, we are able to predictively validate [33], [39]-[40] the response of the numerical MIT model system. The method used for the purpose was non-linear regression modeling, which is also described in terms of ANOVA test results. The sensor IV data for the analysis was taken from the simulations of 15 different sizes of tumor, each at eight different locations, that leads to a total of 240 simulation cases. The maximum sensor reading (out of 240 readings) for the reconstruction of each image is taken and averaged for 8 different locations. This eventually produces only 15 values which correspond to the total number of tumor sizes being studied.

Figure-9 shows that the adjusted R square is 0.998 which indicates that the data fitted are very close to the regression line. Apart from that, the ANOVA analysis also shows a favorable result to the regression model where the F value is more than one (2079.990) and p-value is less than 0.05 (0.00).

| Model summary | | | |
|---|---|---|---|
| R | R Square | Adjusted R Square | Std. Error of the Estimate |
| .999 | .998 | .998 | .016 |

| ANOVA | | | | | |
|---|---|---|---|---|---|
| | Sum of Squares | df | Mean Square | F | Sig. |
| Regression | 1.640 | 3 | .547 | 2079.990 | .000 |
| Residual | .003 | 11 | .000 | | |
| Total | 1.643 | 14 | | | |

| Coefficients | | | | | |
|---|---|---|---|---|---|
| | Unstandardized Coefficients | | Standardized Coefficients | | |
| | B | Std. Error | Beta | t | Sig. |
| Tumor_ Radius | -34.17 | 11.52 | -.45 | -2.97 | .01 |
| Tumor_ Radius ** 2 | -4210.84 | 1645.01 | -.91 | -2.56 | .03 |
| Tumor_ Radius ** 3 | 112057.66 | 67730.72 | .36 | 1.65 | .13 |
| (Constant) | 9.043 | .02 | | 411.29 | .00 |

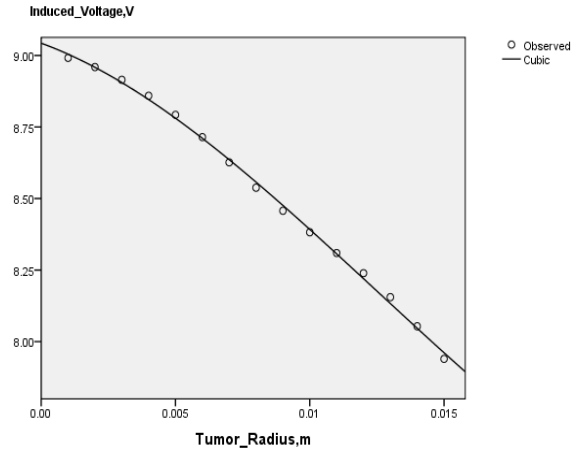


**Figure-9.** SPSS report on cubic regression modeling.

The coefficients table shows the estimated coefficients of the equation of cubic curve fit line that relates the tumor size (radius) with the IV readings. This equation will be useful in predicting the unknown size of a breast tumor. The plot of the cubic fit and actual (observed) IV readings based on the tumor size is also shown.

Despite all the above findings showing relatively good agreement with the theory of magnetic induction, further hardware based measurements should be taken to validate the simulation results prior to planning the manifestations of the method on human breast cancer patients. This is because the simplified 2D version of the human breast and assumptions made on the numerical model could result in deviations to a certain extent. In order to address these issues, further studies will be focused on creating a more realistic 3D MIT system as well as human breast, although experimental validation of the finite element simulation results is the primary objective.

## CONCLUSIONS

This work describes a 2D MIT system with 16 sensor coils for the detection and localization of tumors in the heterogeneous breast tissue. Upon completing the simulation experiments, images of the simulation results were reconstructed using LBP and later were subjected to three different types of error metrics assessment, which are of GREIT standard. Based on the results obtained, it can be concluded that the proposed system can effectively image a breast tumor, which has not been reported in the literature to date. The contactless environment with the breast is the primary nature of the proposed system that made it outperform other upcoming techniques like microwave and EIT techniques. This nature would prevent physical trauma on the patients in the near future; also, it can reduce the unnecessary cost of operation on the shielding material that is to be placed between the patient and the system.

©2006-2016 Asian Research Publishing Network (ARPN). All rights reserved.


**REFERENCES**

[1] A. H. Israyelyan. 2003. The Development of Molecular Diagnostics for Breast Cancer. Louisiana State University.

[2] C. A. Gonzalez, L. M. Lozano, M. C. Uscanga, J. G. Silva and S. M. Polo. 2013. Theoretical and Experimental Estimations of Volumetric Inductive Phase Shift in Breast Cancer Tissue. J. Phys. Conf. Ser. 434: 012004 (4 pp.).

[3] C. A. González. 2012. Simulation of Multi-Frequency Induced Currents in Biophysical Models and Agar Phantoms of Breast Cancer. J. Electromagn. Anal. Appl. 04(08): 317-325.

[4] Z. Zakaria, R. A. Rahim, M. S. B. Mansor, S. Yaacob, N. M. N. Ayob, S. Z. M. Muji, M. H. F. Rahiman, and S. M. K. S. Aman. 2012. Advancements in transmitters and sensors for biological tissue imaging in Magnetic Induction Tomography. Sensors (Switzerland). 12(6): 7126-7156.

[5] Zulkarnay Zakaria. 2014. Magnetic Induction Tomography for Imaging of Steel in Reinforced Concrete Structure. Univerisiti Teknologi Malaysia.

[6] B. Dekdouk. 2010. Image Reconstruction of Low Conductivity Material Distribution using Magnetic Induction Tomography. University of Manchester.

[7] H. Y. W. and M. Soleimani. 2012. Two-Phase Low Conductivity Flow Imaging Using Magnetic Induction Tomography. Prog. Electromagn. Res. 131(no. July): 99-115.

[8] L. Ma. 2014. Magnetic Induction Tomography for Non-destructive Evaluation and Process Tomography. University of Bath, 2014.

[9] Q. Du, B. Bai, P. Pang, and L. Ke. 2012. An improved reconstruction method of MIT based on one-step NOSER. Proc. - 2012 Int. Conf. Biomed. Eng. Biotechnol. iCBEB 2012, no. 1, pp. 723-726.

[10] H. Griffiths, M. Zolgharni, P. D. Ledger and S. Watson. 2010. The cardiff Mk2b MIT head array: Optimising the coil configuration. J. Phys. Conf. Ser. 224: 012046.

[11] J. Caeiros, R. C. Martins and B. Gil. 2012. A new image reconstruction algorithm for real-time monitoring of conductivity and permeability changes in Magnetic Induction Tomography. Conf. Proc. IEEE Eng. Med. Biol. Soc. 2012(1): 6239-6242.

[12] M. Zolgharni. 2010. Magnetic Induction Tomography for Imaging Cerebral Stroke. Swansea University.

[13] M. Zolgharni, H. Griffiths, and P. D. Ledger. 2010. Frequency-difference MIT imaging of cerebral haemorrhage with a hemispherical coil array: numerical modelling. Physiol. Meas. 31(8): S111-25.

[14] M. Zolgharni, H. Griffiths and D. S. Holder. 2009. Imaging haemorrhagic cerebral stroke by frequency-difference magnetic induction tomography : numerical modelling. IFMBE Proc. 49(Figure-2): 2464-2467.

[15] H. Y. Wei and A. J. Wilkinson. 2011. Design of a sensor coil and measurement electronics for magnetic induction tomography. IEEE Trans. Instrum. Meas. 60(12): 3853-3859.

[16] A. M. Mphys. 2004. Image reconstruction in magnetic induction tomography. UWCC.

[17] H. Scharfetter, P. Brunner, and R. Merwa. 2006. Magnetic induction tomography: Solution of the 3-D inverse problem for image reconstruction. Int. J. Inf. Syst. Sci. 2(4): 585-606.

[18] S. Watson, R. J. Williams, W. Gough, and H. Griffiths. 2008. A magnetic induction tomography system for samples with conductivities below 10 S m−1. Meas. Sci. Technol. 19(1): 1-11.

[19] B. Gowry, A.B. Shahriman, Z. Zakaria, R. Ikeura, M.R. Zuradzman, D. Hazry, W.A. Wan Khairunizam, E.M. Cheng. Inductive Phase Shift as a Future Cost Effective Diagnostic Tool in Breast Cancer Localization: A Prologue Study. in International Conference On Advanced Science, Engineering And Technology (ICASET 2015).(Accepted-Unpublished).

[20] K.R. Foster, H. P. Schwan. 1989. Dielectric properties of tissues and biological materials: a critical review. CRC Crit Rev Biomed Eng. 7: 25-104.

[21] Q. Marashdeh and F. L. Teixeira. 2004. Sensitivity matrix calculation for fast 3-D electrical capacitance tomography (ECT) of flow systems. IEEE Trans. Magn. 40(2): 1204-1207.

[22] G. Steiner. 2006. Sequential Fusion of Ultrasound and Electrical Capacitance Tomography. Int. J. Informaion Syst. Sci. 2(4): 484-497.

©2006-2016 Asian Research Publishing Network (ARPN). All rights reserved.


[23] A. Adler, J. H. Arnold, R. Bayford, A. Borsic, B. Brown, P. Dixon, T. J. C. Faes, I. Frerichs, H. Gagnon, Y. Gärber, B. Grychtol, G. Hahn, W. R. B. Lionheart, A. Malik, R. P. Patterson, J. Stocks, A. Tizzard, N. Weiler, and G. K. Wolf. 2009. GREIT: a unified approach to 2D linear EIT reconstruction of lung images. Physiol. Meas. 30(6): S35-S55.

[24] H. Y. Wei and M. Soleimani. 2012. Hardware and software design for a National Instrument-based magnetic induction tomography system for prospective biomedical applications. Physiol. Meas. 33(5): 863-879.

[25] D. Gürsoy, Y. Mamatjan, A. Adler and H. Scharfetter. 2011. Enhancing impedance imaging through multimodal tomography. IEEE Trans. Biomed. Eng. 58(11): 3215-3224.

[26] H. Y. Wei and M. Soleimani. 2012. Theoretical and experimental evaluation of rotational magnetic induction tomography. IEEE Trans. Instrum. Meas. 61(12): 3324-3331.

[27] Z. Wang, A. C. Bovik, H. R. Sheikh and E. P. Simoncelli. 2004. Wavelets for Image Image quality assessment: From error visibility to structural similarity. IEEE Trans. Image Process. 13(4): 600-612.

[28] A. Hore and D. Ziou. 2010. Image Quality Metrics: PSNR vs. SSIM. 2010 20th Int. Conf. Pattern Recognit. pp. 2366-2369.

[29] K. Kipli, S. Krishnan, N. Zamhari, M. S. Muhammad, S. M. W. Masra, K. L. Chin and K. Lias. 2011. Full reference image quality metrics and their performance. 2011 IEEE 7th Int. Colloq. Signal Process. its Appl. 43(12): 33-38.

[30] Z. Wang and A. C. Bovik. 2009. Mean squared error: Lot it or leave it? A new look at signal fidelity measures. IEEE Signal Process. Mag. 26(no. January): 98-117.

[31] A. Daniele, F. Roberto and P. Caterina. 1991, May 10. Calculation of the Dielectric Properties of Body Tissues in the frequency range 10 Hz - 100 GHz [Online]. Available: http://niremf.ifac.cnr.it/tissprop/htmlclie/htmlclie.php.

[32] OriginLab Corporation. 2016. Regression and Curve Fitting. [Online].Available:http://www.originlab.com /doc/Origin-Help/Regression-Curve-Fitting [Accessed: April. 1, 2016]

[33] Hyder A, Buckeridge DL, Leung B. 2013. Predictive Validation of an Influenza Spread Model. PLoSONE8 (6):e65459. doi:10.1371/journal.pone.0065459

[34] Canadian Cancer Society. 2016. Anatomy and physiology of the breast. [Online].Available: http://www.cancer.ca/en/cancer-information/cancer-type/breast/anatomy-and-physiology/?region=on [Accessed: April. 1, 2016].

[35] M. I. Saripan, W. Hidayat, M. Saad, S. Hashim, R. Mahmud, A. J. Nordin, M. A. Mahdi, and S. Member. 2009. Monte Carlo Simulation on Breast Cancer Detection Using Wire Mesh Collimator Gamma Camera. IEEE Trans. Nucl. Sci. 56(3): 1321-1324.

[36] M. N. Lakshmanan, B. P. Harrawood, G. A. Agasthya and A. J. Kapadia. 2014. Simulations of Breast Cancer Imaging Using Gamma-Ray Stimulated Emission Computed Tomography. IEEE Trans. Med. Imaging. 33(2): 546-555.

[37] A. Amina, H.P. Susan and J.W. Anthony. 2016. Potentialities of steady-state and transient thermography in breast tumour depth detection: A numerical study. Comput. Methods Programs Biomed. 3(no. SEPTEMBER 2015): 68-80.

[38] J. Näppi, P. B. Dean, O. Nevalainen and S. Toikkanen. 2001. Algorithmic 3D simulation of breast calcifications for digital mammography. Comput. Methods Programs Biomed. 66(1): 115-124.

[39] M. Martis. 2006. Validation of simulation based models: A theoretical outlook. Electron. J. Bus. Res. Methods. 4(1): 39-46.

[40] H. L. Lew, J. H. Poole, E. H. Lee, D. L. Jaffe, H.C. Huang and E. Brodd. 2005. Predictive validity of driving-simulator assessments following traumatic brain injury: a preliminary study. Brain Inj. 19(3): 177-188.

[41] V. Jochem. 2016, January 20. Biopsy Robot Combines MRI and Ultrasound [Online]. Available: https://www.utwente.nl/en/news/!/2016/1/461204/biopsy-robot-combines-mri-and-ultrasound.

[42] Rebecca L. Siegel, Kimberly D. Miller and J. Ahmedin. 2016. Cancer Statistics. 2016. CA. Cancer J. Clin. 66(1): 7-30.

©2006-2016 Asian Research Publishing Network (ARPN). All rights reserved.


[43] Cancer Research Malyasia. [Online]. Available: http://www.cancerresearch.my/research/breast-cancer/ [Accessed: April. 1, 2016].

[44] H. Stevens. 2016, April 12. Progression of breast cancer: Stages [Online]. Available: http://breast-cancer.ca/prog-untreated/.